energies

MDPI

Article

The Study of a Magnetostrictive-Based Shading Detection Method and Device for the Photovoltaic System

Xiaolei Fu and Yizhi Tian *

School of Electrical Engineering, Xinjiang University, Urumqi 830017, China
* Correspondence: torsionscale@163.com; Tel.: +86-186-9915-6957

Abstract: When the photovoltaic (PV) system suffers shading problems caused by different degrees and areas, the shaded PV cells will consume electricity and generate heat, the corresponding bypass diode operating at a certain current will conduct, and a special magnetic field will be generated in space. In this study, a magnetostrictive-based shading detection method and device for the PV system are developed from theoretical, simulation, and physical experimental aspects. This study aims to detect the special magnetic field using magnetostrictive material with a certain response pattern under the magnetic field to detect and locate the shading problem of each module in the PV system. Theoretically, the analysis is carried out from the on–off situation of the bypass diodes of PV modules under different shading conditions and the response mechanism of magnetostrictive materials under the action of the magnetic field. During simulation, the finite element magnetic field simulations are performed for the diode and the series magnetic field coil, and the structural parameters of the magnetic field coil are designed based on the simulation results. After establishing the validation idea of the detection method in this study, the experimental platform is built and the experimental steps are designed. Finally, the feasibility of the method proposed in this study is verified, the detection range of the method is calculated, and the minimum spacing of adjacent magnetic field coils is determined by experimental validation. This study provides a novel magnetostrictive-based detection method, as well as a theoretical and experimental basis, for identifying and localizing PV system shading problems, and discusses the feasibility of shading detection at the system level.

Keywords: PV system shading detection; PV module bypass diode; magnetostrictive sensor; finite element magnetic field simulation

Citation: Fu, X.; Tian, Y. The Study of a Magnetostrictive-Based Shading Detection Method and Device for the Photovoltaic System. *Energies* **2023**, *16*, 2906. https://doi.org/10.3390/en16062906

Academic Editors: Annamaria Buonomano, Jayanta Deb Mondol and Biplab Das

Received: 11 February 2023
Revised: 13 March 2023
Accepted: 17 March 2023
Published: 21 March 2023

1. Introduction

In compliance with immense modern energy demands, the need for a cheaper and reliable energy supply is globally evolving. In global energy resource utilization, renewable energy, such as biomass, hydrogen, solar radiation, and wind speed, is considered to be a promising means of solving problems associated with the rise in alternatives to fossil fuels, environment pollution, and global temperature, [1]. Photovoltaic (PV) technologies have been widely and maturely used in the market and will play a leading role in the current energy transition in order to address the disadvantages of environmental issues posed by fossil fuels. The highest contribution of currently installed PV systems is identified in Asia, including China (175 GW), Japan (55.5 GW), and India (26.8 GW). Europe ranks second in terms of PV-installed capacity, with considerable shares in Germany (45.9 GW), Italy (20.12 GW), and the UK (13.4 GW) as of 2020 [2]. The currently available PV technologies possess less than 23% conversion efficiencies, which underlines the need for further improvements to ensure better technological competitiveness [3].

1.1. Definition of the Shading Problem

In the PV system, every PV array consists of PV strings connected in parallel, every PV string consists of PV modules connected in series, and every PV module consists of PV

cells connected in series. Over the last few years, traditional crystalline PV technologies have mostly been applied to new PV power plants [4]. When the surface of a single PV cell or different PV cells receives uneven illumination, this situation is referred to as a shading problem [5]. In actual operation, PV cells are often affected by clouds, dust, trees, buildings, etc., and suffer from shading problems [6].

When a PV cell has a certain degree and area of shading problem, its output power decreases, and the output current shows a downward trend [7]. Due to the special structure of the PV string, the rest of the normal PV module outputs a current of the original size to the shaded PV module, resulting in a large amount of power consumption on the shaded PV modules, an abnormal temperature rise, and a further "hot spot effect" [8]. The frequent occurrence of the "hot spot effect" will cause irreversible damage to the internal physical structure and external packaging materials of PV modules, which will seriously affect the reliability and service life of PV modules and even endanger the normal operation of the whole PV system [9].

The addition of bypass diodes connected in reverse parallel to the output of each PV module is proposed to protect PV modules from operating at negative voltages [10]. When a PV module has shading problems, its bypass diodes provide a shunt path for the rest of the normal PV modules in the string, which reduces the negative impact of the shading problems on the PV system to a certain extent, but the shading problems still exist and cannot be located [11]. Due to the non-linear output characteristics of PV cells, the PV system needs to monitor the output power of PV arrays and provide maximum power point tracking (MPPT) [12]. In the uniform irradiance condition, the PV strings only have a single maximum power point (MPP). Due to the use of the bypass diodes, a portion of the PV modules located in shadow or at lower irradiance will cause multiple peaks in the output power of the PV string, which is not conducive to achieving MPPT and causes energy loss [13]. Therefore, successfully detecting and locating shading problems can help to improve the safety and output power of the PV system.

1.2. The Prior Technical Ideas for PV Shading Detection

Among the prior technical ideas for PV shading detection, these studies focus on the output characteristics of PV strings. The authors of [14] proposed a detection method to classify the PV strings into four working conditions based on the real electrical measurements. The authors of [15], based on the instantaneous current reduction between PV strings and MPPT sampling instants, proposed a sensor-less detection technique to monitor the output characteristics of the PV strings. The authors of [16] proposed an improved sine–cosine algorithm to find a periodic partial shading condition and a MPP, avoiding the local power point obstacle. The authors of [17] considered the meteorological data as input variables and the coordinates of the MPP as targets, and also used artificial neural networks to detect the presence of partial shading and infer the number of shaded PV modules. The above studies successfully identified shading problems in PV strings in PV arrays, but could not pinpoint the shading problem to each PV module.

These studies focus on the shading conditions of individual PV modules. The authors of [18] proposed a method and sensor to detect partial shading on a module during its MPPT operation. The authors of [19] proposed using dynamic reconfiguration to rearrange the connection structure of PV modules by controlling electrical switches to maximize the output power and realize shading detection. The above studies successfully identified the shading problems in individual PV modules, but the signal lines of the sensors or switches for each module could not pinpoint the shading problem on each PV module, which complicated the whole PV system.

These studies revolve around the image recognition of photovoltaic arrays. The literature [20] proposes the use of webcams to identify the shadow irradiance and provide the reference voltage of the MPP using image analysis techniques. In the literature [21], an artificial neural network tool for image recognition is proposed to quantify the power loss caused by shading and the hot spot effects of PV modules. The studies mentioned above

successfully identified the shading problems of individual PV modules by uncomplicated equipment composition, but there are limitations due to weather, distance, and image capture angles. The literature [22] proposes the use of unmanned aerial vehicles to capture the images of PV arrays for judging the shading condition of each PV module. The literature [23] proposes the use of fully convolutional networks with depth training for improving the recognition accuracy of aerial images of PV arrays. The above literature solves some of the limitations compared to the solution using fixed camera devices, but does not allow for the real-time detection of shading conditions.

1.3. The Study Ideas in This Paper

Based on the structure of the connection between the PV module and the bypass diode, as well as the shunting effect of the bypass diode when the PV module has shading problems, after finding the correspondence between the shading problems and the on–off state of bypass diodes, if we identify and locate the bypass diodes under on-state conditions, we can then successfully detect shading problems. The literature [24] verified that the short circuit of the bypass diode would cause a power loss in systems due to the mismatch phenomenon, and the reverse current would create electro-thermal problems in the PV array. Due to the electro-magnetic effect, the magnetic field is instantaneous and homogeneous compared to the heat when the diode is conducting. Therefore, this study aims to successfully recognize PV shading problems via the real-time detection of the magnetic field generated when the bypass diode is under on-state conditions.

In the process of magnetization, the size of the magnetic material elongates or shortens in the direction of magnetization, i.e., the magnetostrictive effect [25]. The magnetostrictive displacement sensor made by this effect enables the non-contact long-distance detection of multiple magnetic fields [26]. In the literature [27], a magnetostrictive sensor with a 50 m range is proposed for detecting the liquid level.

In summary, the specific study idea of this paper is as follows. The special distribution of magnetic fields is considered in space when the bypass diodes of PV modules are turned on under different degrees and areas of shading conditions. The response pattern of magnetostrictive materials are studied under the action of this magnetic field, the detection device is developed, and the shading problems of PV modules are identified and localized.

2. Materials and Methods

2.1. Analysis of the Diode On–Off Situation

The 300 W PV module is taken as an example from the current model. After 20 PV cells are connected in series to form a substring, 3 substrings are connected in series to form a PV module. One bypass diode is connected in reverse parallel to the output of each substring, and, finally, the bypass diode and its connecting wires are concentrated in the junction box. When a substring appears with shaded cells, this substring is referred to as the shaded substring. The internal wiring structure of the 300 W PV module is shown in Figure 1 [28].

As shown in Figure 2, within the same substring, the output current I_n and voltage U_r of the PV cell in normal conditions operate in the first quadrant. When a PV cell has a short-circuit current drop due to shading, the output current I_n of the normal PV cells in series with it is higher, resulting in the higher reverse bias voltage U_r of the shaded cell, whose current–voltage curve works in the second quadrant, consuming power and generating a certain amount of heat.

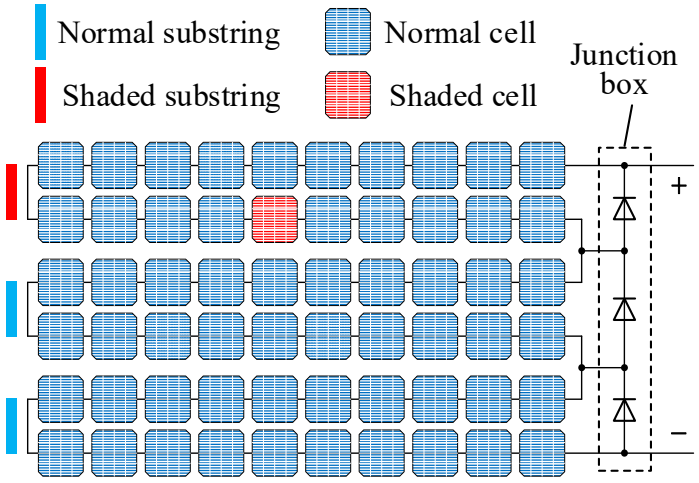

Figure 1. The internal wiring structure of the 300 W PV module.

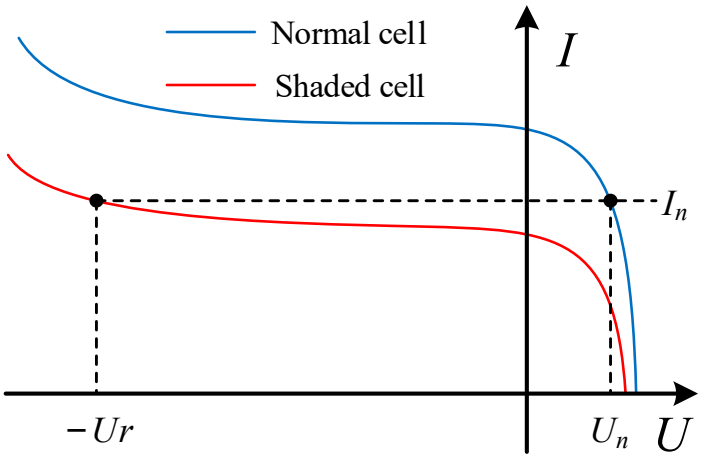

Figure 2. Current–voltage curves of normal and shaded cells in the same substring.

The on–off state of the bypass diode is analyzed. Assuming that there is one shaded cell in the substring and the rest are normal cells, the bypass diode will turn on when the output voltage of the substring is reverse-biased and higher than the conduction voltage of the bypass diode U_d. Thus, the following is satisfied [29]:

$$U_r - 19U_n \geq U_d \tag{1}$$

As shown in Figure 3, I_s is the short-circuit current of the normal substring and cell, I_{rc} is the short-circuit current of the shaded substring, I_g is the short-circuit current of the shaded cell, and U_{rc} is the critical reverse bias voltage of the shaded cell when the diode is switched on.

When the operating current of the substring is in interval 1, the output voltage of all cells within the substring operates is found in the first quadrant. Each cell outputs power, and each diode is switched off.

When the operating current of the substring is in interval 2, the shaded cell consumes power because its output voltage is reverse-biased. However, the output voltage of the substring is still in the first quadrant, making Equation (1) not valid and the diode is still switched off. Therefore, the current range in this interval is referred to as the bypass diode operating blind zone.

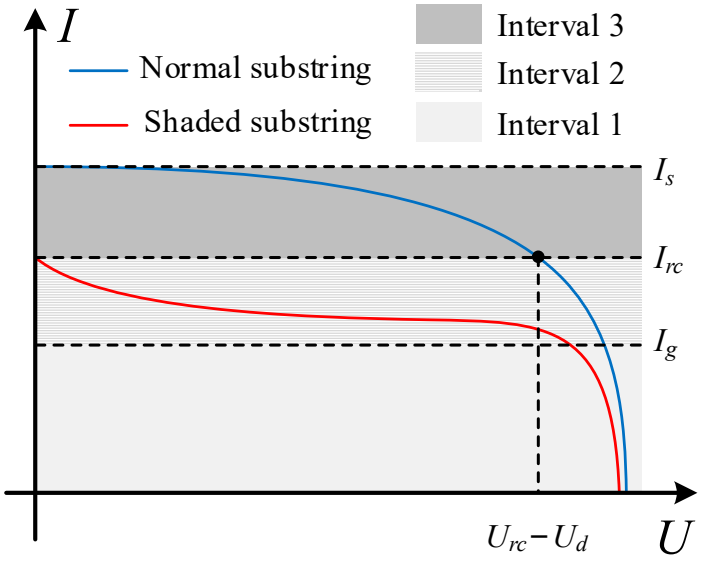

Figure 3. Current–voltage curves of normal and shaded substrings in the same PV module.

When the operating current of the substring is in interval 3, the output voltage of the shaded cell is reverse-biased and exceeds the critical value U_{rc}, so that Equation (1) becomes valid, and thus the diode conducts. Therefore, an appropriate increase in the operating current can turn on the bypass diode that works in the operating blind zone.

According to the results of the above analysis, due to the special wiring structure inside the PV module, the on–off state of the bypass diode is related to the interval where the operating current of the PV module is located under shading conditions.

By adjusting the operating current of the PV string, the bypass diode of the corresponding PV substring turns on and generates a specific magnetic field at a spatial location when there is a shading problem in the PV string. Detecting and locating this magnetic field helps to identify and localize the shading problems.

2.2. Analysis of the Response Mechanism of Magnetostrictive Materials under the Specific Magnetic Field Environment

Magnetostrictive materials are characterized by high permeability, low coercivity, easy magnetization, easy demagnetization, and small hysteresis line envelope area, which can be used to detect the location of specific magnetic fields in space over long distances. Under the action of the magnetic field, the length of magnetostrictive material in the direction of magnetic inductance changes from l_o to l and satisfies [30]:

$$\lambda = \frac{l - l_o}{l_o} \tag{2}$$

In Equation (2), λ is the line magnetostriction coefficient, which can be classified as a positive or negative magnetostriction coefficient according to its plus or minus value. The magnetostriction coefficient of a magnetostrictive material at saturation magnetic induction intensity is called the saturation magnetostriction coefficient λ_s.

The magnetostrictive waveguide wire with radius r has a uniform cross-sectional current distribution when a pulse current with amplitude I_c and pulse width τ passes, and the surface current density J can be expressed as:

$$J = \frac{I_c}{\pi r^2} \tag{3}$$

According to Ampere's law of circulation, the current I passing through a circular section of radius a inside the waveguide wire, with the axis as the center, is [31]:

$$I = J\pi a^2 = \frac{I_c a^2}{r^2} = \oint_C H \cdot dl = 2H\pi a \tag{4}$$

Furthermore, the intensity of the pulsed magnetic field H inside the waveguide wire at the position of distance a from the axis is obtained as:

$$H = \frac{I_c a}{2\pi r^2} \tag{5}$$

Equation (5) shows that the pulsed magnetic field is highest at the surface position of the waveguide wire with the value H_c:

$$H_c = \frac{I_c}{2\pi r} \tag{6}$$

The relative magnetic permeability of the waveguide wire surface when only subjected to the pulsed magnetic field is μ_{r1}. Based on the value of absolute magnetic permeability μ_0 of vacuum as $4\pi \times 10^{-7}$ Wb/(A·m), the pulsed magnetic induction intensity B_{c1} can be calculated as [32]:

$$B_{c1} = \frac{H_c}{\mu_0 \mu_{r1}} = \frac{I_c}{2\pi r \mu_0 \mu_{r1}} \tag{7}$$

Under the action of this magnetic induction intensity B_{c1}, the magnetostriction coefficient of the waveguide wire is λ_1, the circumferential magnetostriction deformation produced on the surface of the waveguide wire is Δl_1, and the original circumference of the circular section of the waveguide wire is l_0. Thus, the following is satisfied:

$$\lambda_1 = \frac{\Delta l_1}{l_0} = \frac{\Delta l_1}{2\pi r} \tag{8}$$

The magnetic induction intensity distribution on the surface of the waveguide wire can be analyzed when a permanent magnet generating axial magnetic field exists at the local position of the waveguide wire. With the center of the waveguide wire cross-section circle as the origin, the axial direction of the waveguide wire as the y-axis direction, and the waveguide wire cross-section as the plane where the xz-axis is located, a right-angle coordinate system is established, as shown in Figure 4.

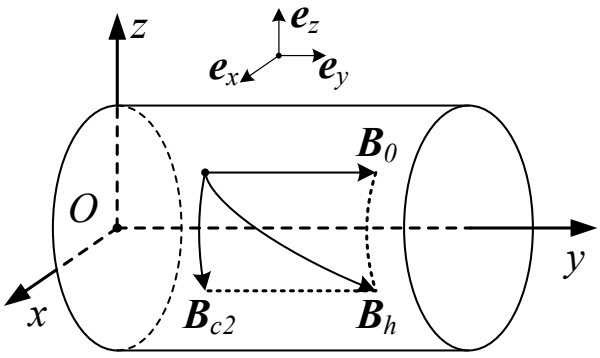

Figure 4. The magnetic induction vector distribution on the surface of the waveguide wire.

Taking the first quadrant of the xyz axis as an example, the coordinates of a point on the surface of the waveguide wire can be expressed as:

$$\left(x, y, \sqrt{r^2 - x^2}\right) \tag{9}$$

The magnetic induction intensity vector generated within the waveguide wire when subjected only to the constant axial magnetic field of the permanent magnet is $\mathbf{B}_0$, which is expressed as:

$$\mathbf{B}_0 = \mathbf{B}_0 \mathbf{e}_y \tag{10}$$

In Equation (10), $\mathbf{e}_y$ denotes the unit magnetic induction intensity vector in the positive direction of the y-axis. Under the action of magnetic induction intensity $\mathbf{B}_0$, the relative magnetic permeability of the waveguide wire is μ_{r2}. By substituting the coordinate point (9) to Equation (7), the pulse magnetic induction intensity vector $\mathbf{B}_{c2}$ at this point can be expressed as:

$$\mathbf{B}_{c2} = \frac{I_c}{2\pi r \mu_0 \mu_{r2}} \cdot \left(\frac{\sqrt{r^2 - x^2}}{r} \mathbf{e}_x - \frac{x}{r} \mathbf{e}_z \right) \tag{11}$$

By superimposing the axial magnetic induction intensity vector $\mathbf{B}_0$ with the circumferential pulse magnetic induction intensity vector $\mathbf{B}_{c2}$, the torsional magnetic induction intensity vector $\mathbf{B}_h$ is calculated as follows:

$$\mathbf{B}_h = \frac{I_c \sqrt{r^2 - x^2}}{2\pi r^2 \mu_0 \mu_{r2}} \mathbf{e}_x + \mathbf{B}_0 \mathbf{e}_y - \frac{I_c x}{2\pi r^2 \mu_0 \mu_{r2}} \mathbf{e}_z \tag{12}$$

In Equation (12), $\mathbf{e}_x$, $\mathbf{e}_y$, and $\mathbf{e}_z$ denote the unit magnetic induction intensity vectors in the positive direction of the x, y, and z axes, respectively. Under the action of torsional magnetic induction intensity B_h, the magnetostriction coefficient of the waveguide wire is λ_2.

During the action of the circumferential pulsed magnetic induction intensity vector $\mathbf{B}_{c2}$, the axial magnetic induction intensity vector $\mathbf{B}_0$ does not change, so the direction of magnetostrictive deformation on the surface of the waveguide wire remains circumferential. The deformation variable Δl_2 generated by the torsional magnetic field acting on the surface of the waveguide wire can be expressed as:

$$\lambda_2 = \frac{\Delta l_2}{l_0} = \frac{\Delta l_2}{2\pi r} \tag{13}$$

When the waveguide wire is mechanically stretched and fixed at both ends without allowing its deformation, a shear stress σ will be generated on the surface of the waveguide wire and transmitted along the waveguide wire in the form of a torque wave.

The shear modulus of the waveguide wire is G. According to the shear Hooke law, the relationship between the shear stress σ and the relative deformation variable Δl can be expressed as [33]:

$$\sigma = G\Delta l = G(\Delta l_2 - \Delta l_1) \tag{14}$$

Substituting Equations (8) and (13) into Equation (14) yields:

$$\sigma = 2\pi r G(\lambda_2 - \lambda_1) \tag{15}$$

The initial permeability of the waveguide wire in the absence of magnetic field influence is μ_{r0}, the permeability of its surface under the action of the shear stress σ is μ_σ, the saturation magnetic induction intensity of the waveguide wire material is B_s, and the corresponding saturation magnetostriction coefficient is λ_s. Then, according to the inverse magnetostriction effect, the following relationship exists between the change in the permeability of the waveguide wire and the stress applied to the waveguide wire [34]:

$$\frac{\mu_{r0} - \mu_\sigma}{\mu_\sigma} = \frac{2\lambda_s}{B_s} \sigma \mu_{r0} \tag{16}$$

From Equation (16), it can be deduced that:

$$d\mu = \mu_{r0} - \mu_\sigma = \frac{2\lambda_s \mu_{r0} \mu_\sigma}{B_s} d\sigma \tag{17}$$

Substituting Equation (15) into Equation (17) yields:

$$d\mu = \frac{4\pi r G \lambda_s \mu_{r0} \mu_\sigma}{B_s} d\lambda \tag{18}$$

A detection coil is installed along the axial direction of the waveguide wire, at a position far from the permanent magnet L, to detect the torque wave generated by the shear stress σ. By combining a permanent magnet with magnetic field intensity H_L with the detection coil, the magnetic induction intensity B_L induced by the waveguide wire with absolute permeability μ at the position of the detection coil satisfies:

$$B_L = \mu H_L \tag{19}$$

Substituting Equation (19) into Equation (18) yields:

$$dB_L = \frac{4\pi r G \lambda_s \mu_{r0} \mu_\sigma H_L}{B_s} d\lambda \tag{20}$$

According to Faraday's law of electromagnetic induction, the number of turns of the detection coil is N, and the area of the coil facing the magnetic field is S. Therefore, the induced electromotive force E caused by the transmission of the torque wave to the detection coil is:

$$E = NS \cdot \frac{dB_L}{dt} \tag{21}$$

Substituting Equation (20) into Equation (21) yields:

$$E = \frac{4\pi r G N S \lambda_s \mu_{r0} \mu_\sigma H_L}{B_s} \cdot \frac{d\lambda}{dt} \tag{22}$$

The magnetostriction coefficients of the waveguide wire are λ_1 and λ_2 when the pulsed magnetic induction intensity B_{c1} and the torsional magnetic induction intensity B_h are acting on the waveguide wire, respectively. Substituting them with the pulse width τ of the pulsed current into Equation (22) yields:

$$E = \frac{4\pi r G N S \lambda_s \mu_{r0} \mu_\sigma H_L (\lambda_2 - \lambda_1)}{\tau B_s} \tag{23}$$

The transmission speed of the torque wave is v. Based on the transmission time t of the torque wave from the position of the permanent magnet to the detection coil, the position information of the permanent magnet L can be further calculated as [35]:

$$L = vt \tag{24}$$

Since the transmission speed of the torque wave is a constant on the waveguide wire, the torque wave generated from multiple permanent magnet positions at different distances can be transmitted sequentially to the detection coil. Wave-absorbing rubbers are installed at both ends of the waveguide wire to reduce signal interference, thus enabling the non-contact long-distance detection of multiple magnetic fields.

According to Equation (23), it can be seen that the induced electromotive force E of the detection coil is positively related to the amount of variation in the magnetostriction coefficient of the waveguide wire at the position of the permanent magnet, so the axial magnetic field generated by the permanent magnet is the key influencing factor.

According to the simulation results in Figures 5 and 6, the size and direction of this magnetic field are not uniformly distributed, and are vulnerable to interference from the magnetic field generated by the internal energized conductor of the junction box and the external PV cells at work. This is not conducive to the direct detection of this magnetic field by magnetostrictive material.

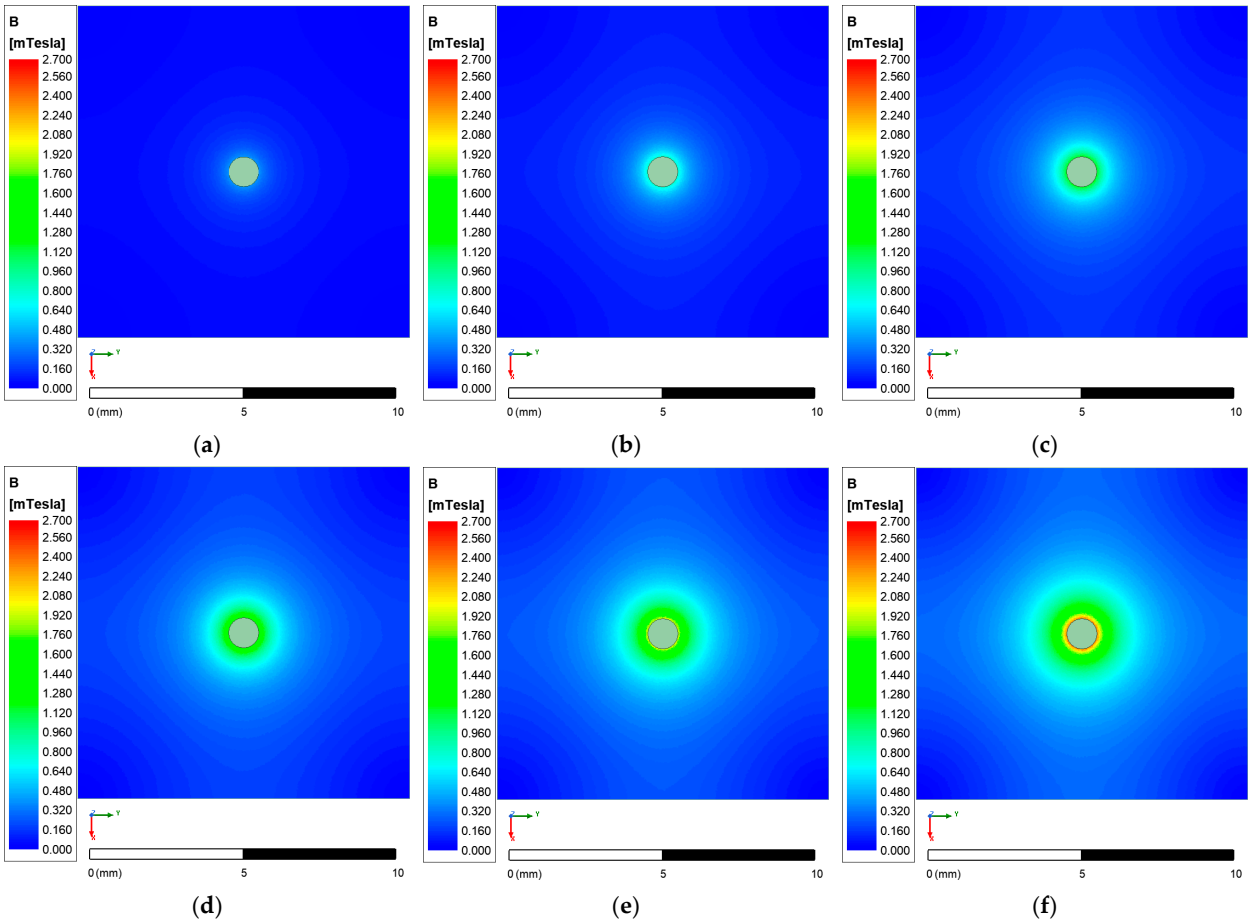

Figure 5. The results of the magnetic field simulation for the diode pin line when the diode is conducting at (**a**) 1A, (**b**) 2A, (**c**) 3A, (**d**) 4A, (**e**) 5A, and (**f**) 6A.

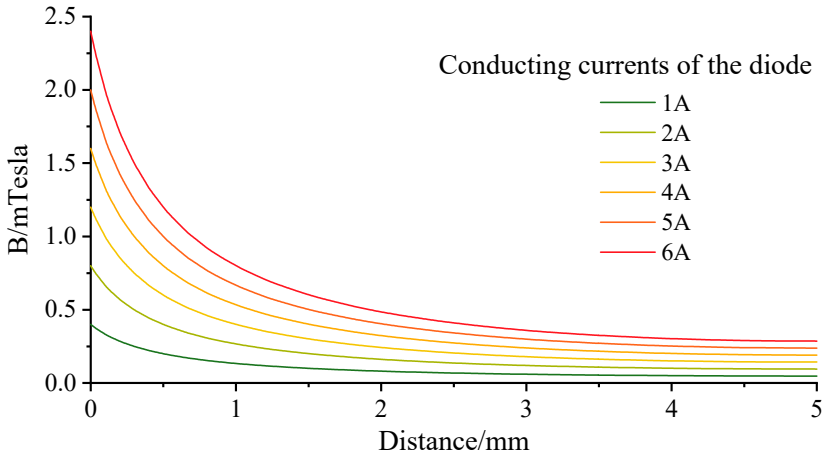

Figure 6. The curves indicating the relationship between the magnetic induction intensity and the distance in space to the surface position of the diode pin line.

2.3. Finite Element Simulation Analysis of the Magnetic Field Distribution When the Diode Is under On-State Conditions

Before the magnetic field simulation of the conduction diode, it is necessary to select a suitable type of PV module as the experimental object and then select the type of bypass diode. To facilitate the study of the protection role of bypass diodes in multi-substring PV modules, the single-substring PV module consisting of 12 PV cells connected in series is selected as the experimental object. Its type and parameters are selected, as shown in Table 1.

Table 1. The type and parameters of the experimental PV module.

Parameters	Type Specification or Numerical Value
Type specification	Monocrystalline PV module
Number of cells	12
Number of substrings	1
Number of bypass diodes	1
Maximum power	100 W
Open-circuit voltage	21.5 V
Short-circuit current	5.85 A
Maximum power operating voltage	18 V
Maximum power operating current	5.41 A
Dimension	920 × 670 mm^2

The type and parameters of the corresponding bypass diode, are selected as shown in Table 2.

Table 2. The type and parameters of the bypass diode.

Parameters	Type Specification or Numerical Value
Type specification	10A10MIC rectifier diode
Material of the pin line	Tinned copper
Diameter of the pin line	1.0 mm
Maximum forward current	10 A
Maximum forward voltage	1.1 V
Peak reverse voltage	700 V

According to the parameters listed in Table 2 and the actual installation position of the diode in the junction box on the backside of the PV module, the physical model of the diode pin line is established in the ANSYS 2020 R2 software (Canonsburg, PA, USA). Using the axial direction of the pin line as the *z*-axis direction and the cross-section of the pin line as the plane where the *xy*-axis is located, the maximum power operating currents of the PV modules (1, 2, 3, 4, 5, and 6 A) are selected as the on-state currents of the diode for magnetic field simulation, and the simulation results are shown in Figure 5.

The curve corresponding to the values of different distances in space to the surface position of the diode pin line and the simulation result of the magnetic induction intensity *B* is shown in Figure 6.

The simulation results in Figures 5 and 6 show that the spatial magnetic induction intensity at 1 mm from the diode pin line is less than 1.0 mT when the diode is used with 6 A as the on-state current. According to the above magnetic field simulation results, considering that the on–off state of each bypass diode in the whole PV string is affected by different shading conditions and conduction currents, magnetostrictive material with a certain response pattern under the action of the magnetic field is chosen to detect the special magnetic field.

2.4. Structure Design of Coil Connected in Series with the Diode

To increase the magnetic field strength generated by the current in the branch where the bypass diode is conducting and to distribute it more uniformly in a fixed direction,

part of the conductor inside the branch is designed as a coil structure. The coil is densely winded so that the adjacent wire turns are closely spaced to reduce magnetization leakage after conduction. The coil of this structure is called the magnetic field coil.

Enameled copper wire is selected as the winding material. The winding length of the magnetic field coil is l_x, the inner radius is r_x, the diameter of the enameled wire is d_x, the diameter of the winding copper core is d_{Cu}, the cross-sectional area of the winding copper core is S_{Cu}, the thickness of the lacquer coating is d_s, and the maximum number of winding layers is m.

According to the maximum safe load current J_{Cu} of copper, the short-circuit current 5.85 A of the PV module is chosen as the maximum on-state current I_{dm} of the branch where the coil is located, and the maximum cross-sectional area of the copper core $S_{Cu\max}$ is calculated as:

$$S_{Cu\max} = \frac{I_{dm}}{J_{Cu}} \tag{25}$$

The corresponding minimum diameter of copper core $d_{Cu\max}$ is:

$$d_{Cu\max} = \sqrt{\frac{4S_{Cu\max}}{\pi}} = \sqrt{\frac{4I_{dm}}{\pi J_{Cu}}} \tag{26}$$

When the bypass diode is conducted with the maximum value I_{dm}, the minimum equivalent resistance of the diode $R_{\min}$ is calculated based on the on-state voltage U_{dm}:

$$R_{\min} = \frac{U_{dm}}{I_{dm}} \tag{27}$$

The forward conduction current–voltage curve of the 10A10MIC rectifier diode is shown in Figure 7.

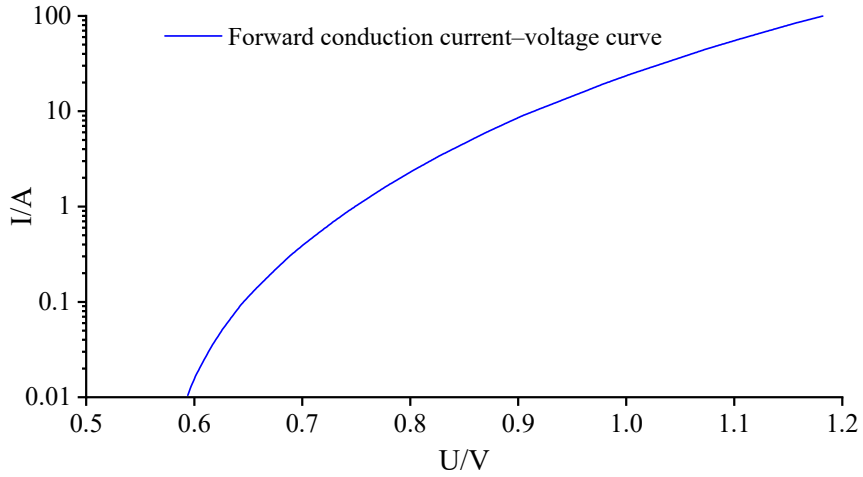

Figure 7. The forward conduction current–voltage curve of the 10A10MIC rectifier diode.

Based on the forward conduction current–voltage curve of the diode in Figure 7, the parameters in Equation (27) are selected and calculated, as shown in Table 3.

Table 3. The on-state voltage and equivalent resistance of the diode corresponding to the maximum on-state current.

Parameters	Numerical Value	Unit
Maximum on-state current I_{dm}	5.85	A
Corresponding on-state voltage U_{dm}	0.865	V
Minimum equivalent resistance $R_{\min}$	0.148	Ω

To reduce the impact of the magnetic field coil in the branch circuit due to voltage division on the protective effect of the diode, its maximum resistance value $R_{x\max}$ should be much smaller than the minimum equivalent resistance value of the diode $R_{\min}$. Thus, the following is satisfied:

$$100R_{x\max} \leq R_{\min} \tag{28}$$

According to the resistivity ρ_{Cu} of copper, the maximum winding length of the coil wire $l_{x\max}$ is satisfied:

$$l_{x\max} = \frac{R_{\min}S_{Cu\max}}{100\rho_{Cu}} = \frac{\pi R_{\min}d_{Cu\max}^2}{400\rho_{Cu}} \tag{29}$$

The number of each layer turns of the magnetic field coil winding can be calculated to be 1 and the perimeter of each layer can be calculated. The maximum value of the winding length $l_{x\max}$ and the maximum number of winding layers m satisfy:

$$l_{x\max} \geq 2\pi m r_x + \pi m^2 d_x \tag{30}$$

According to the above calculation process, the winding length $l_{x\max}$ limits the structure of the magnetic field coil, and the selection and calculation results of the parameters in relation to the magnetic field coil are shown in Table 4.

Table 4. The selection and calculation results of the parameters related to the magnetic field coil.

Parameters	Numerical Value	Unit
The maximum safe load current density J_{Cu} of copper	5.2	A/mm^2
The resistivity ρ_{Cu} of copper	0.0185	Ω mm^2/m
The inner radius r_x of coil	0.75	mm
The diameter d_{Cu} of copper core	1.22	mm
The thickness d_s of lacquer coating	0.04	mm
The diameter d_x of enameled wire	1.28	mm
The maximum resistance value $R_{x\max}$	1.48	mΩ
The winding length $l_{x\max}$	90	mm
The maximum number m of winding layers	4	/

According to the parameters of Table 4, the maximum number of winding layers m is calculated in correspondence to the number of each layer turns. In the ANSYS finite element simulation software, the physical models are built sequentially, and 5.41 A is selected as the magnetic field coil conduction current I_d to characterize the operating current.

The maximum value of magnetic induction intensity $B_{x\max}$ at the position of the magnetic field coil central axis is recorded, according to the magnetic field simulation results. According to the calculation and simulation results, the corresponding curve between the maximum value of magnetic induction intensity $B_{x\max}$ and the serial number of structures of magnetic field coil is shown in Figure 8.

The specific numerical correspondence between the maximum value of magnetic induction intensity $B_{x\max}$, the serial number of the structure, the total turns, and the number of each layer turns is shown in Table 5.

According to the simulation results, it can be seen that the maximum value of magnetic induction intensity $B_{x\max}$ generated at the position of the magnetic field coil central axis is the largest when the on-state current is the same and the 5th winding structures of 3 turns in layer 1, 2 turns in layer 2, and 1 turn in layer 3 are used. Based on this winding structure, experiments are carried out to verify the method used in this paper.

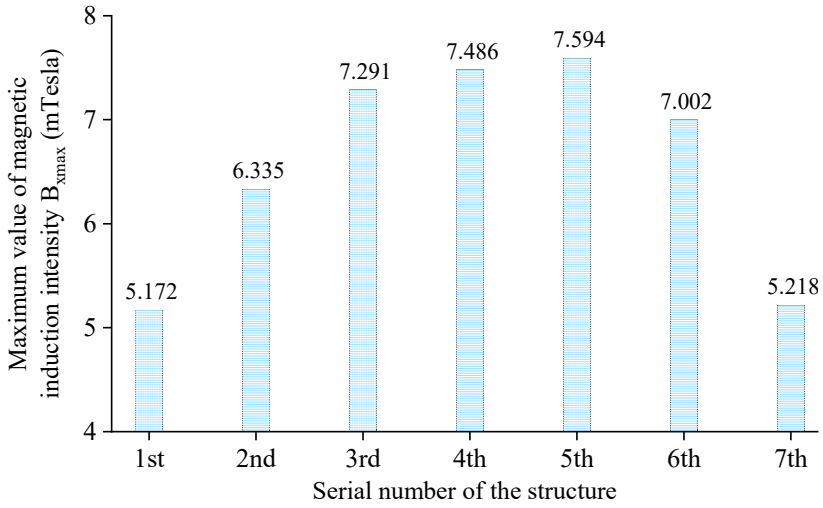

Figure 8. The correspondence curve between the winding structures of the magnetic field coil and the maximum value of magnetic induction.

Table 5. The numerical correspondence between the structure of each winding of the magnetic field coil and the maximum value of magnetic.

Serial Number of the Structure	Total Turns	Layer				B_{xmax} (mT)
		1st	2nd	3rd	4th	
1st	10	10	0	0	0	5.172
2nd	9	8	1	0	0	6.335
3rd	8	6	2	0	0	7.291
4th	6	3	3	0	0	7.486
5th	6	3	2	1	0	7.594
6th	7	5	1	1	0	7.002
7th	4	1	1	1	1	5.218

3. Results and Discussion

3.1. Validation Idea of the Experiment

As shown in Figure 9, to verify the magnetostrictive-based PV system shading detection method used in this paper, the experimental equipment to be used includes PV modules, bypass diodes, magnetic field coils, a voltage controller, a resistive load, a pulse power supply, pulse signal lines, waveguide wire, a detection coil, and an oscilloscope.

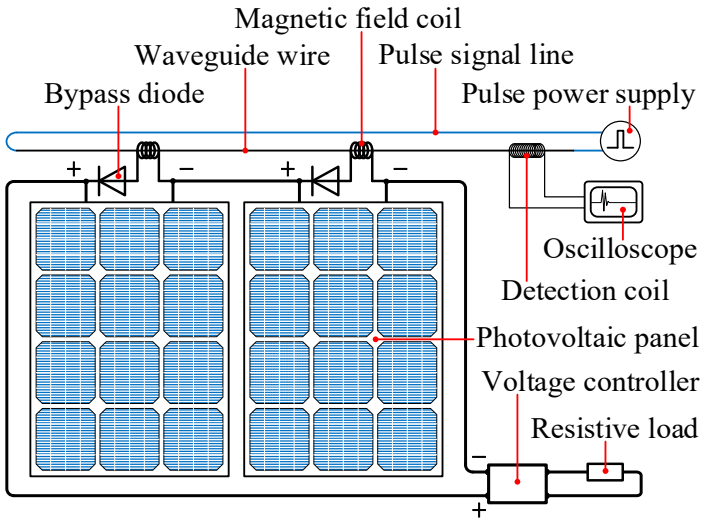

Figure 9. The relationship between each piece of experimental equipment.

The process of the whole detection method is shown in Figure 10.

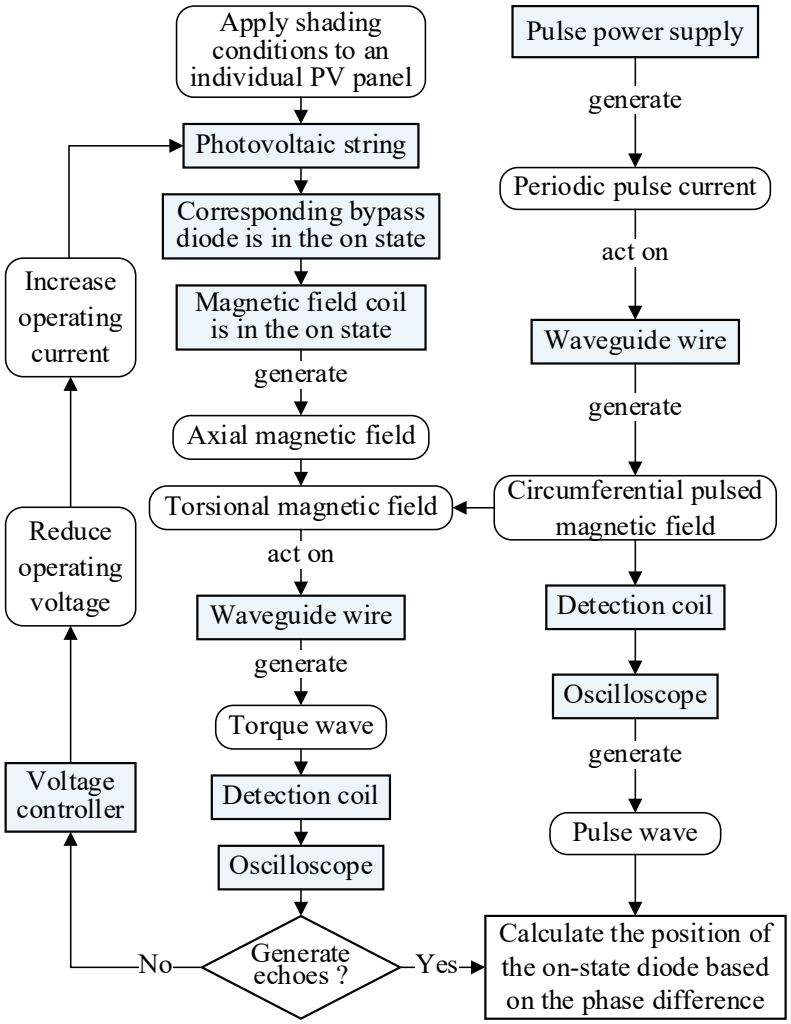

Figure 10. The process of the whole detection method.

Two PV modules are connected in series to form a PV string, and shading conditions are applied to single PV modules so that its corresponding bypass diode conducts and generates a local axial magnetic field from the magnetic field coil. This magnetic field is superimposed on the pulsed circumferential magnetic field generated when the waveguide wire is passed with a periodic pulsed current to form a torsional magnetic field.

Under the action of the torsional magnetic field, the waveguide wire produces a torque wave that propagates to both ends from the corresponding position. The magnetic field change caused by the end-position waveguide wire under the action of the pulse current and torque wave is detected by the detection coil, and the output waveform of the induced electromotive force generated by the detection coil is collected using an oscilloscope.

Based on the phase difference between the pulse wave and the corresponding echo, the specific position of the PV module corresponding to the magnetic field coil in the on-state current can be calculated.

3.2. Construction of the Experimental Platform

As shown in Figure 11, the experimental platform consists of two series-connected PV modules and their junction boxes, a DC voltage–current meter, a DC boost converter, a resistive load, a waveguide wire, signal lines, a pulse power supply, a detection coil, and an oscilloscope.

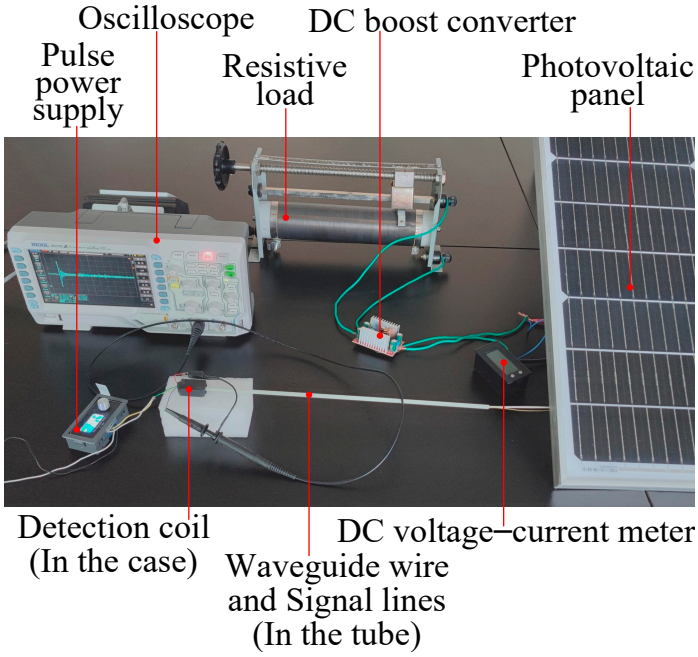

Figure 11. The experimental platform.

In the experimental platform, the magnetic field coil is connected in series with the branch where the bypass diode is in the junction box at the back of the PV module. The output of the PV module string is connected to the input of the DC boost converter and the resistive load is connected to the output of the DC boost converter. The waveguide wire passes through the detection coil and the magnetic field coils in turn and forms a circuit in series with the pulse power supply through signal lines. The output of the detection coil is connected to the probes of the oscilloscope. Wave-absorbing rubbers are installed at the ends of the waveguide wire to reduce the interference caused by the rebound torque waves transmitted from the end position of the waveguide wire.

The type and parameters of the PV module are shown in Table 1. The type and parameters of the bypass diode are shown in Table 2. The iron–nickel alloy is selected as the material for the waveguide wire with the specific dimensional parameters shown in Table 6.

Table 6. The dimensional parameters of the waveguide wire.

Parameters	Numerical Value	Unit
Length	3	m
Diameter	0.8	mm

Since the pulse signal is critical to the generation of the torque waves, the difference in the amplitude, width, duration, and period of the pulse affects the amplitude and stability of the output voltage waveform from the detection coil; thus, it is necessary to experimentally determine the appropriate pulse signal.

The PWM pulse generator is selected as the signal source of the pulse power supply, and a direct current of 4A is selected on the magnetic field coil for conduction purposes. The maximum peak echo is induced by the detection coil when the pulse amplitude is selected as 12 V.

According to the output characteristics of the PWM pulse generator and the interference between different echoes, the echo duration is the shortest when the pulse width is chosen as 5 μs and the pulse duration is chosen as 20 μs.

It takes time for the torque wave to propagate to the detection coil from the time it is generated. The torque wave needs to be received before the next pulse signal is generated,

so the pulse period needs to be greater than the maximum time for the torque wave to be received. The period of the pulse signal is experimentally chosen as 20 ms.

The finalized output waveform of pulse power is shown in Figure 12.

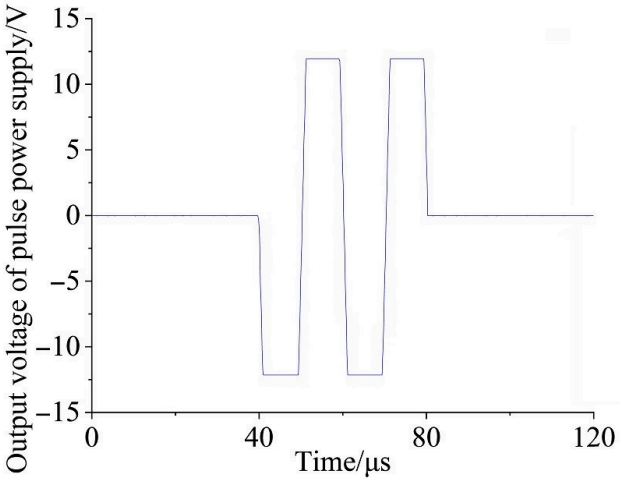

Figure 12. The output waveform of the pulse power.

3.3. Design of the Experimental Steps

The experiments based on the above experimental platform include PV shading experiment and magnetic field detection experiment.

3.3.1. PV Shading Experiment

The experimental platform is placed in a light environment and shading conditions are imposed on the individual PV module. The output voltage of the PV module string is changed by the DC boost converter, the reading of the DC voltage–current meter is recorded, and the output current–voltage and output power–voltage curves of the PV module string are plotted.

The testing device needs to run throughout the entire experiment. During the one-way recording of the PV module string output voltage growth from zero to open-circuit voltage, when the acquired waveform graph of the oscilloscope no longer shows any echoes, the output current of the PV module string is recorded at this time as the critical on-current value of the bypass diode under this masking condition.

3.3.2. Magnetic Field Detection Experiment

The minimum value of the operating current corresponding to the maximum power point of the PV module string under each shading condition is used as the on-state current of the magnetic field coil.

The distance between the magnetic field coil and the detection coil is changed, the echo acquisition is observed in the waveform graph collected by the oscilloscope, and the speed of torque wave propagation along the waveguide wire and the detection range of the method used are calculated in this paper. The separation distance of two magnetic field coils is changed and the minimum separation distance of adjacent magnetic field coils is calculated by observing the interference situation of echoes in the waveform graph collected by the oscilloscope.

3.4. Results and Analysis of the PV Shading Experiment

A sunny day at noon is selected as the experimental time, the experimental platform is placed in the outdoor light environment, and the PV module string is determined with the ground at an angle of 30° inclination. White paper is selected as a slight shade with low light transmittance and thick cardboard is selected as a heavy shade with no light transmittance. One PV module is kept in normal operation and different areas of lateral

or longitudinal shading are applied to an individual cell in the other PV module while changing the output voltage of the PV module string and recording the readings of the DC voltage–current meter. To minimize the influence of the error caused by the change in light intensity and temperature on the experiment, each set of experimental data is measured within 15 min.

The PV module string output current–voltage curves for different degrees and areas of shading conditions when shading is applied laterally are shown in Figure 13a, and the output power–voltage curves are shown in Figure 13b. When the shading conditions are applied longitudinally, the corresponding output current–voltage curve is shown in Figure 13c and the output power–voltage curve is shown in Figure 13d.

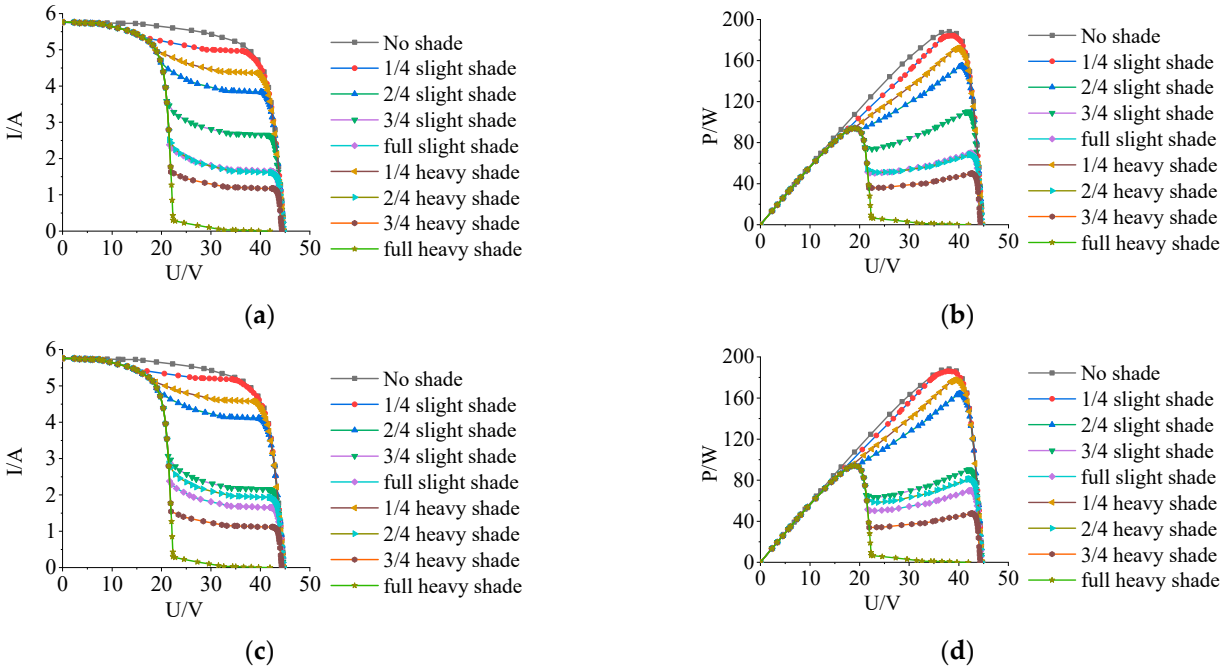

Figure 13. The output current–voltage and power–voltage curves of the PV module string in (**a**,**b**) lateral and (**c**,**d**) longitudinal shading conditions.

The maximum power point current of the PV module string is used as the operating current of the diode.

When the critical conduction current of the diode is greater than the operating current, the oscilloscope acquires no echo in the waveform graph, i.e., when the diode operates under off-state conditions. When the critical conduction current of the diode is less than the operating current, the oscilloscope acquires echoes in the waveform graph, i.e., when the diode operates under on-state conditions.

The corresponding relationships between the maximum power point current of the PV module string and the bypass diode on–off state and critical conduction currents under each shading condition are shown in Table 7.

Table 7. The bypass diode on–off state in each shading condition.

Shading Conditions	Maximum Power Point Current	Numerical Value	The On–Off State of Diode during Maximum Power Operation
No shade	4.948	/	off
Lateral 1/4 slight	4.726	5.342	off
Longitudinal 1/4 slight	4.931	5.479	off
Lateral 2/4 slight	3.814	4.650	off
Longitudinal 2/4 slight	4.089	4.896	off
Lateral 3/4 slight	2.634	3.546	off

Table 7. *Cont.*

Shading Conditions	Maximum Power Point Current	Numerical Value	The On–Off State of Diode during Maximum Power Operation
Longitudinal 3/4 slight	4.849	3.105	on
Full slight	4.831	2.360	on
Lateral 1/4 heavy	4.338	4.995	off
Longitudinal 1/4 heavy	4.553	5.131	off
Lateral 2/4 heavy	4.822	2.549	on
Longitudinal 2/4 heavy	4.852	2.796	on
Lateral 3/4 heavy	4.811	1.641	on
Longitudinal 3/4 heavy	4.834	1.538	on
Full heavy	4.859	0.302	on

According to the analysis results from Figure 3 and the information in Table 7, when the shading degree and area of an individual PV cell are small and the PV module string is operating at the maximum power point, the operating current of the PV module string is higher than the critical on-state current of the bypass diode, which restrains the bypass diode in the operating blind zone.

Therefore, appropriately increasing the operating current in a short period can make the bypass diode, originally found in the blind area, conduct, and further analyzing the echoes that appear in the waveform graph collected by the oscilloscope can help to realize the troubleshooting and positioning of potential shading problems.

3.5. Results and Analysis of the Magnetic Field Detection Experiment

The pulse current is conducted to the waveguide wire. After amplifying and limiting the output voltage waveform signal of the detection coil, the oscilloscope is used for acquisition and analysis.

When the magnetic field coil does not conduct, the waveform acquired by the oscilloscope is shown in Figure 14.

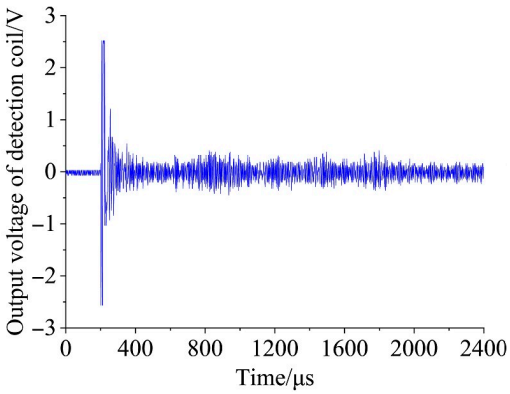

Figure 14. The waveform acquired by the oscilloscope when the magnetic field coil is not conducted.

The signal waves with peaks above 1 V in the figure show the pulse wave and the initial echo. The pulsed wave is caused by changes in the magnetic field when the waveguide wire conducts a pulsed current. The initial echo within 100 μs after the pulse wave is caused by the initial torque wave generated by the waveguide wire at the signal line connection position after the pulse current is applied.

The minimum value of the current corresponding to the maximum power point of the PV module string in Table 7 (2.634 A) is selected as the on-state current of the magnetic field coil. By adjusting the distance between the magnetic field coil and the detection coil, the effective waveforms acquired by the oscilloscope are shown in Figure 15a–c, respectively, when the magnetic field coil is placed at the head, middle, and end positions of the waveguide wire in turn after conducting.

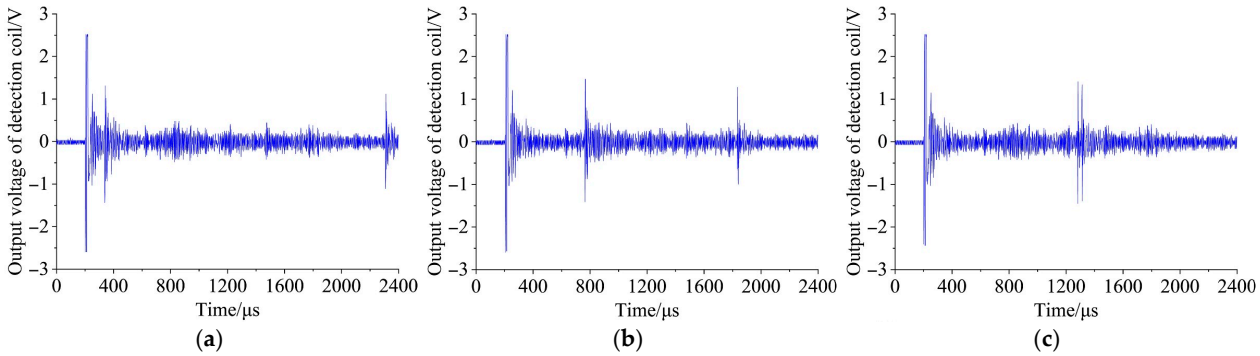

Figure 15. The waveform acquired by the oscilloscope when the magnetic field coil is conducting at the (**a**) head, (**b**) middle, and (**c**) end positions of the waveguide wire.

The signal waves with peaks above 1 V in the figures show the pulse wave, the initial echo, the target echo, and the elastic wave. The target echo is caused by the torque wave generated at the position corresponding to the waveguide wire after the magnetic field coil is turned on, with a minimum signal peak value of 1.28 V. The elastic wave is caused by the rebound torque wave generated after the torque wave is transmitted to the end of the waveguide wire, and its signal peak is smaller than that of the target echo.

Figure 15 shows that when the magnetic field coil is located at the position of the waveguide wire head, the time interval between the peak of the target echo and the pulse wave should be greater than 100 μs to reduce the interference of the initial echo. The pulse wave is the starting point, the midpoint of the horizontal line connecting the target echo peak and the elastic wave peak is the endpoint, and the interval time between the two points is 1080 μs. Therefore, waveform signals with peaks greater than 1.28 V and located within 100–1080 μs after the pulse wave are considered valid target echoes.

Based on the length of the waveguide wire of 3 m, the actual speed of the torque wave propagation along the waveguide wire is calculated as 2778 m/s. It is further calculated that the detection range of the method used in this paper is 0.28–3.00 m, and its maximum detection range is the same as the length of the waveguide wire.

After conducting the two magnetic field coils simultaneously with 2.634 A of direct current, the spacing distance of the magnetic field coils is adjusted so that there is no superposition effect between the target echo signals collected by the oscilloscope. The effective waveform graph acquired by the oscilloscope at the minimum interval distance is shown in Figure 16.

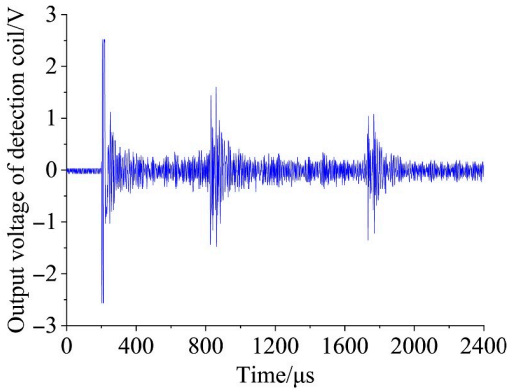

Figure 16. The effective waveform graph acquired by the oscilloscope when adjacent magnetic field coils reach the minimum interval distance.

In Figure 16, the torque waves generated by the conduction of the two magnetic field coils, after causing the two target echoes in turn, are rebounded by the end of the

waveguide wire, causing an elastic wave of the same time interval. To observe the details of the time interval between the two target echoes in the figure, a local zoom is performed at the target echoes position, as shown in Figure 17.

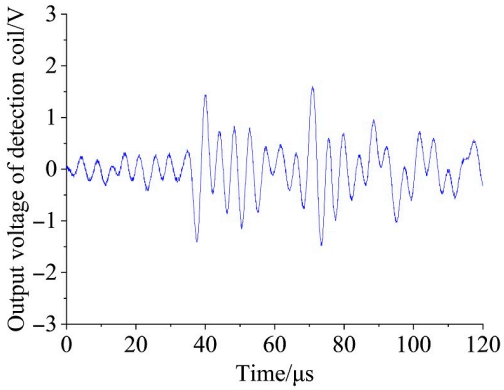

Figure 17. The details of the waveform acquired by the oscilloscope when adjacent magnetic field coils are at the minimum interval distance.

According to Figure 17, the minimum time interval between two adjacent target echoes is 31 μs. Based on the propagation speed of the torque wave along the waveguide wire, the minimum separation distance between adjacent magnetic field coils is calculated as 86 mm. After several groups of experiments are verified, excluding any invalid data caused by improper operation, the detection error of the experimental device is 4 mm, so the installation distance of the magnetic field coil is not affected by this error.

In summary, in the actual installation of the detection equipment designed in this paper, the distance between the first magnetic field coil and the detection coil should be greater than 0.28 m, and the interval distance between adjacent magnetic field coils should be greater than 86 mm.

4. Conclusions

The size and structural parameters of the magnetic field coil are determined based on the results of the magnetic field simulation. By building an experimental platform, the output waveform of the induced voltage of the detection coil is calculated and analyzed based on the conclusion of the analysis of the diode on–off situation in the PV shading experiment. The feasibility of the detection method is verified, the detection range of the method is calculated, and the minimum spacing of adjacent diodes corresponding to the magnetic field coils is determined. This study proposes a novel detection method based on magnetostriction and offers a theoretical and experimental basis for the shading problem of the PV system.

When the PV module is shaded by a smaller degree and area, if the operating current of the PV module is higher than the critical on-current of the bypass diode, the bypass diode will work in the blind area and remain off, which is not conducive to detection.

The PV string voltage controller is studied so that the bypass diode, originally found in the blind area of operation, can be conducted by appropriately increasing the operating current for a short period. Further magnetic field detection and localization are performed by magnetostrictive sensors to enable the identification and localization of potential shading problems. Specifically, it needs to be paired with a control algorithm that performs maximum power tracking while selecting moments of fixed period to increase the operating current of the PV string. During this period, the magnetostrictive sensors in this paper keep working and finally achieve MPPT, while monitoring the operating status of each PV module in the PV array in real time.

5. Patent

Tian, Y.; Wei, B.; Fu, X. A Shielded Condition Monitoring and Recognition Device for PV Modules Based on Magnetostriction. Xinjiang Uygur Autonomous Region. CN114285376A, 5 April 2022.

Author Contributions: Conceptualization, Y.T.; methodology, X.F.; software, X.F.; validation, X.F.; formal analysis, X.F.; investigation, X.F.; data curation, X.F.; writing—original draft preparation, X.F.; writing—review and editing, Y.T. and X.F.; visualization, Y.T.; supervision, Y.T.; project administration, Y.T.; funding acquisition, Y.T. All authors have read and agreed to the published version of the manuscript.

Funding: This research was funded by the Natural Science Foundation of Xinjiang Uygur Autonomous Region (2022D01C364).

Data Availability Statement: The data are available from the corresponding author upon reasonable request.

Acknowledgments: The authors acknowledge the technical support of the School of Electrical Engineering, Xinjiang University.

Conflicts of Interest: The authors declare no conflict of interest.

Nomenclature

PV	photovoltaic
MPP	the maximum power point
MPPT	the maximum power point tracking
I_n	the output current of the PV cell in normal conditions
U_r	the output voltage of the PV cell in normal conditions
U_r	the reverse bias voltage of the shaded PV cell
U_d	the conduction voltage of the bypass diode
I_s	the short-circuit current of the normal PV cell
I_{rc}	the short-circuit current of the shaded PV cell
I_g	the short-circuit current of the shaded PV cell
U_{rc}	the critical reverse bias voltage of the shaded PV cell
l_o	the original length of magnetostrictive material
l	the present length of magnetostrictive material
λ	the line magnetostriction coefficient
λ_s	the saturation magnetostriction coefficient
r	the radius of the magnetostrictive waveguide wire
I_c	the amplitude of the pulse current
τ	the pulse width
J	the density of the surface current
a	the radius of the waveguide wire
H	the intensity of the pulsed magnetic field
H_c	the intensity of the pulsed magnetic field at the position of the waveguide wire surface
μ_{r1}	the relative magnetic permeability of waveguide wire surface when subjected only to the pulsed magnetic field
μ_0	the absolute magnetic permeability of the vacuum
B_{c1}	the pulsed magnetic induction intensity
λ_1	the magnetostriction coefficient of the waveguide wire
l_0	the original circumference of the circular section of the waveguide wire
$\mathbf{B}_0$	the axial magnetic induction intensity vector
$\mathbf{B}_{c2}$	the circumferential pulse magnetic induction intensity vector
$\mathbf{B}_h$	the torsional magnetic induction intensity vector
$\mathbf{e}_x$	unit magnetic induction intensity vectors in the positive direction of the x axis
$\mathbf{e}_y$	unit magnetic induction intensity vectors in the positive direction of the y axis
$\mathbf{e}_z$	unit magnetic induction intensity vectors in the positive direction of the z axis

λ_2	the magnetostriction coefficient of the waveguide wire under the action of torsional magnetic induction intensity
σ	the shear stress
G	the shear modulus
Δl	the deformation variable of the waveguide wire
μ_{r0}	the initial permeability of the waveguide wire in the absence of magnetic field influence
μ_σ	the permeability of the waveguide wire under the action of the shear stress
B_s	the saturation magnetic induction intensity of the waveguide wire
λ_s	the saturation magnetostriction coefficient
L	the position information of the permanent magnet
H_L	the magnetic field intensity of the permanent magnet
B_L	the magnetic induction intensity induced by the waveguide wire from the permanent magnet
μ	the absolute permeability
N	the number of turns of the detection coil
S	the area of coil facing the magnetic field
E	the induced electromotive force of the detection coil
v	the transmission speed of the torque wave
t	the transmission time of the torque wave
l_x	the winding length of the magnetic field coil
r_x	the inner radius of the magnetic field coil
d_x	the diameter of the enameled wire
d_{Cu}	the diameter of the winding copper core
S_{Cu}	the cross-sectional area of the winding copper core
d_s	the thickness of the lacquer coating
m	the maximum number of winding layers
J_{Cu}	the maximum safe load current of copper
I_{dm}	the maximum on-state current of the magnetic field coil
$S_{Cu\max}$	the maximum cross-sectional area of the copper core
$d_{Cu\max}$	the minimum diameter of the copper core
$R_{\min}$	the minimum equivalent resistance of the diode
U_{dm}	the maximum on-state voltage of the magnetic field coil
$R_{x\max}$	the maximum resistance of the magnetic field coil
ρ_{Cu}	the resistivity of copper
$l_{x\max}$	the maximum winding length of the coil wire
I_d	the conduction current of the magnetic field coil
$B_{x\max}$	the maximum magnetic induction intensity at the position of the magnetic field coil central axis

References

1. Saha, S.; Saini, G.; Mishra, S.; Chauhan, A.; Upadhyay, S. A comprehensive review of techno-socio-enviro-economic parameters, storage technologies, sizing methods and control management for integrated renewable energy system. *Sustain. Energy Technol. Assess.* **2022**, *54*, 102849. [CrossRef]
2. Allouhi, A.; Rehman, S.; Buker, M.S.; Said, Z. Up-to-date literature review on Solar PV systems: Technology progress, market status and R&D. *J. Clean. Prod.* **2022**, *362*, 132339. [CrossRef]
3. Alami, A.H.; Rabaia, M.K.H.; Sayed, E.T.; Ramadan, M.; Abdelkareem, M.A.; Alasad, S.; Olabi, A.G. Management of potential challenges of PV technology proliferation. *Sustain. Energy Technol. Assess.* **2022**, *51*, 101942. [CrossRef]
4. Zsiboracs, H.; Zentko, L.; Pinter, G.; Vincze, A.; Baranyai, N.H. Assessing shading losses of photovoltaic power plants based on string data. *Energy Rep.* **2021**, *7*, 3400–3409. [CrossRef]
5. Vunnam, S.; VanithaSri, M.; RamaKoteswaraRao, A. Performance analysis of mono crystalline, poly crystalline and thin film material based 6 × 6 T-C-T PV array under different partial shading situations. *Optik* **2021**, *248*, 168055. [CrossRef]
6. Saiprakash, C.; Mohapatra, A.; Nayak, B.; Ghatak, S.R. Analysis of partial shading effect on energy output of different solar PV array configurations. *Mater. Today Proc.* **2021**, *39*, 1905–1909. [CrossRef]
7. Bressan, M.; Gutierrez, A.; Gutierrez, L.G.; Alonso, C. Development of a real-time hot-spot prevention using an emulator of partially shaded PV systems. *Renew. Energy* **2018**, *127*, 334–343. [CrossRef]
8. Tang, S.; Xing, Y.; Chen, L.; Song, X.; Yao, F. Review and a novel strategy for mitigating hot spot of PV panels. *Sol. Energy* **2021**, *214*, 51–61. [CrossRef]

9. Skomedal, Å.F.; Aarseth, B.L.; Haug, H.; Selj, J.; Marstein, E.S. How much power is lost in a hot-spot? A case study quantifying the effect of thermal anomalies in two utility scale PV power plants. *Sol. Energy* **2020**, *211*, 1255–1262. [CrossRef]
10. Bastidas-Rodríguez, J.D.; Ramos-Paja, C.A.; Serna-Garcés, S.I. Improved modelling of bypass diodes for photovoltaic applications. *Alex. Eng. J.* **2022**, *61*, 6261–6273. [CrossRef]
11. Kreft, W.; Przenzak, E.; Filipowicz, M. Photovoltaic chain operation analysis in condition of partial shading for systems with and without bypass diodes. *Optik* **2021**, *247*, 167840. [CrossRef]
12. Jha, V. Generalized modelling of PV module and different PV array configurations under partial shading condition. *Sustain. Energy Technol. Assess.* **2023**, *56*, 103021. [CrossRef]
13. Ragb, O.; Bakr, H. A new technique for estimation of photovoltaic system and tracking power peaks of PV array under partial shading. *Energy* **2023**, *268*, 126680. [CrossRef]
14. Fadhel, S.; Delpha, C.; Diallo, D.; Bahri, I.; Migan, A.; Trabelsi, M.; Mimouni, M.F. PV shading fault detection and classification based on I-V curve using principal component analysis: Application to isolated PV system. *Sol. Energy* **2019**, *179*, 1–10. [CrossRef]
15. Li, C.; Yang, Y.; Zhang, K.; Zhu, C.; Wei, H. A fast MPPT-based anomaly detection and accurate fault diagnosis technique for PV arrays. *Energy Convers. Manag.* **2021**, *234*, 113950. [CrossRef]
16. Chandrasekaran, K.; Sankar, S.; Banumalar, K. Partial shading detection for PV arrays in a maximum power tracking system using the sine-cosine algorithm. *Energy Sustain. Dev.* **2020**, *55*, 105–121. [CrossRef]
17. Salem, F.; Awadallah, M.A. Detection and assessment of partial shading in photovoltaic arrays. *J. Electr. Syst. Inf. Technol.* **2016**, *3*, 23–32. [CrossRef]
18. Seapan, M.; Hishikawa, Y.; Yoshita, M.; Okajima, K. Detection of shading effect by using the current and voltage at maximum power point of crystalline silicon PV modules. *Sol. Energy* **2020**, *211*, 1365–1372. [CrossRef]
19. Sugumar, S.; Winston, D.P.; Pravin, M. A novel on-time partial shading detection technique for electrical reconfiguration in solar PV system. *Sol. Energy* **2021**, *225*, 1009–1025. [CrossRef]
20. Martin, A.D.; Vazquez, J.R.; Cano, J.M. MPPT in PV systems under partial shading conditions using artificial vision. *Electr. Power Syst. Res.* **2018**, *162*, 89–98. [CrossRef]
21. Cavieres, R.; Barraza, R.; Estay, D.; Bilbao, J.; Valdivia-Lefort, P. Automatic soiling and partial shading assessment on PV modules through RGB images analysis. *Appl. Energy* **2022**, *306*, 117964. [CrossRef]
22. Di Tommaso, A.; Betti, A.; Fontanelli, G.; Michelozzi, B. A multi-stage model based on YOLOv3 for defect detection in PV panels based on IR and visible imaging by unmanned aerial vehicle. *Renew. Energy* **2022**, *193*, 941–962. [CrossRef]
23. Sizkouhi, A.M.; Aghaei, M.; Esmailifar, S.M. A deep convolutional encoder-decoder architecture for autonomous fault detection of PV plants using multi-copters. *Sol. Energy* **2021**, *223*, 217–228. [CrossRef]
24. Lee, C.G.; Shin, W.G.; Lim, J.R.; Kang, G.H.; Ju, Y.C.; Hwang, H.M.; Chang HSKo, S.W. Analysis of electrical and thermal characteristics of PV array under mismatching conditions caused by partial shading and short circuit failure of bypass diodes. *Energy* **2021**, *218*, 119480. [CrossRef]
25. Ahmed, U.; Jeronen, J.; Zucca, M.; Palumbo, S.; Rasilo, P. Finite element analysis of magnetostrictive energy harvesting concept device utilizing thermodynamic magneto-mechanical model. *J. Magn. Magn. Mater.* **2019**, *486*, 165275. [CrossRef]
26. Seco, F.; Martin, J.M.; Jimenez, A.R.; Calderon, L. A high accuracy magnetostrictive linear position sensor. *Sens. Actuators A Phys.* **2005**, *123*, 216–223. [CrossRef]
27. Magnetostrictive liquid-level sensors. *Ultrasonics* **1967**, *5*, 196. [CrossRef]
28. Ko, S.W.; Ju, Y.C.; Hwang, H.M.; So, J.H.; Jung, Y.S.; Song, H.J.; Song, H.E.; Kim SHKang, G.H. Electric and thermal characteristics of photovoltaic modules under partial shading and with a damaged bypass diode. *Energy* **2017**, *128*, 232–243. [CrossRef]
29. Teo, J.C.; Tan, R.H.; Mok, V.H.; Ramachandaramurthy, V.K.; Tan, C. Impact of bypass diode forward voltage on maximum power of a photovoltaic system under partial shading conditions. *Energy* **2020**, *191*, 116491. [CrossRef]
30. Deng, C.; Kang, Y.; Li, E.; Zhang, Y.; Cheng, J.; Ge, T. A new model of the signal generation mechanism on magnetostrictive position sensor. *Measurement* **2014**, *47*, 591–597. [CrossRef]
31. Tarasov, V.E. General non-local electrodynamics: Equations and non-local effects. *Ann. Phys.* **2022**, *445*, 169082. [CrossRef]
32. Wang, H.; Yang, W.; Huang, Y. Adaptive finite element method for two-dimensional time-harmonic magnetic induction intensity equations. *J. Comput. Appl. Math.* **2022**, *412*, 114319. [CrossRef]
33. Shrikanth, S.; Neelakantan, S.; Prasad, R. Planes of Isotropic shear moduli in anisotropic materials. *Mech. Mater.* **2023**, 104619. [CrossRef]
34. Bechtold, C.; Teliban, I.; Thede, C.; Chemnitz, S.; Quandt, E. Non-contact strain measurements based on inverse magnetostriction. *Sens. Actuators A Phys.* **2010**, *158*, 224–230. [CrossRef]
35. Seco, F.; Martín, J.M.; Pons, J.L.; Jiménez, A.R. Hysteresis compensation in a magnetostrictive linear position sensor. *Sens. Actuators A Phys.* **2004**, *110*, 247–253. [CrossRef]